Demixing the miscible liquids: toward biphasic battery electrolytes based on the kosmotropic effect†

Won-Yeong Kim, ‡[a] Hong-I Kim,‡[b] Kyung Min Lee,‡[b] Eunhye Shin,[b] Xu Liu, [cd] Hyunseok Moon,[a] Henry Adenusi, [e] Stefano Passerini, *[cd] Sang Kyu Kwak *[f] and Sang-Young Lee *[a]

Exploring new electrolyte chemistry beyond conventional single-phase battery electrolytes is needed to fulfill the heterogeneous requirements of anodes and cathodes. Here, we report a biphasic liquid electrolyte (BLE) based on the kosmotropic effect. The key underlying technology for the BLE is phase separation of its electrolyte couples using a principle of "demixing the miscible liquids". Kosmotropic/chaotropic anions affect the ion coordination structures and the intermolecular interactions of electrolyte couples, enabling on-demand control of their immiscibility/miscibility. Despite the intrinsic miscibility of water (in aqueous electrolytes) and acetonitrile (in nonaqueous electrolytes), the structural change of the aqueous electrolyte induced by kosmotropic anions allows demixing with the nonaqueous electrolyte. The resultant BLE facilitates redox kinetics at cathodes and Zn plating/stripping cyclability at anodes. Consequently, the BLE enables Zn-metal full cells to exhibit a long cyclability (86.6% retention after 3500 cycles). Moreover, Zn anode-free full cells with the BLE exhibit a higher energy density (183 W h kg^{-1}) than previously reported Zn batteries.

Broader context

Battery electrodes require optimal operating environments to facilitate individual electrochemical activities. To address this issue, new electrolyte chemistry should be explored in addition to electrode material development. Most electrolytes reported to date have been based on single-phase characteristics, resulting in difficulties for simultaneously fulfilling the heterogeneous requirements of anodes and cathodes. Herein, we report a biphasic liquid electrolyte (BLE) based on the kosmotropic effect. The key underlying technology for the BLE is phase separation of its electrolyte couples (aqueous and nonaqueous electrolytes) using a principle of "demixing the miscible liquids". The BLE improves redox kinetics at cathodes and Zn plating/stripping cyclability at anodes, resulting in long cycling and a high energy density (183 W h kg^{-1} for a Zn anode-free cell). This BLE strategy holds promise as a versatile electrolyte synthesis platform that can address long-unresolved performance limitations of battery electrodes.

Introduction

The ongoing surge in demand for advanced batteries with fully-fledged electrochemical performance spurs us to explore new vistas of electrochemistry and materials chemistry.[1] In principle, anodes and cathodes of batteries, which are, respectively, designed to undergo different types of electrochemical reactions, necessitate their own optimal operating environments (*e.g.*, redox potentials and electrolyte polarity) in order to ensure individual electrochemical activities.[2] These chemical and electrochemical challenges in the electrodes strongly rely on electrolytes which serve as an ionic medium in batteries, thus inspiring the pursuit of new electrolyte systems that enable stable interfaces with electrodes and provide facile ion transport.[3]

[a] *Department of Chemical and Biomolecular Engineering, Yonsei University, 50 Yonsei-ro, Seodaemun-gu, Seoul 03722, Republic of Korea. E-mail: syleek@yonsei.ac.kr*

[b] *Department of Energy Engineering, School of Energy and Chemical Engineering, Ulsan National Institute of Science and Technology (UNIST), Ulsan 44919, Republic of Korea*

[c] *Helmholtz Institute Ulm (HIU), Helmholtzstraße 11, 89081, Ulm, Germany*

[d] *Karlsruhe Institute of Technology (KIT), P.O. Box 3640 D-76021, Karlsruhe, Germany. E-mail: stefano.passerini@kit.ed*

[e] *Hong Kong Quantum AI Lab (HKQAI), 17 Science Park West Avenue, Hong Kong 999077, China*

[f] *Department of Chemical and Biological Engineering, Korea University, 145 Anam-ro, Seongbuk-gu, Seoul 02841, Republic of Korea. E-mail: skkwak@unist.ac.kr*

† Electronic supplementary information (ESI) available: Fig. S1–S38, Tables S1–S8, Notes S1–S5, and Video S1. See DOI: https://doi.org/10.1039/d2ee03077b

‡ These authors contributed equally to this work.

Numerous approaches have been implemented to develop new electrolytes, with a focus on synthesis and engineering of new salts/solvents,[4 6] functional additives,[7] high-salt-concentration electrolytes,[8] and composition optimization.[9] Unfortunately, most of these electrolytes reported to date have been based on single-phase characteristics, resulting in difficulties for simultaneously fulfilling the ever-intensifying heterogeneous requirements of anodes and cathodes. To resolve this challenge, biphasic electrolytes composed of two different electrolytes have been proposed,[10 17] including the use of solvent pairs with opposite polarities[10 15] and the introduction of thick ion-conducting barriers (*e.g.*, lyophobic polymeric membranes[16] and solid-state inorganic electrolytes[17]) to physically isolate two miscible electrolytes. However, a biphasic electrolyte incorporating a nonpolar solvent shows low ionic conductivity because of its insufficient dissociation ability. In addition, the ion-conducting barriers often require complex cost-consuming synthetic processes, and their large thickness causes the inevitable loss of cell energy density as well as inferior rate performance. These limitations of the previous studies are mainly attributed to their biased approaches to bulk properties of biphasic electrolyte constituents. Therefore, a bottom-up design of biphasic electrolytes is needed based on the understanding of their molecular chemistry and intermolecular interactions.

Here, we present a class of biphasic liquid electrolytes (BLEs) based on the kosmotropic effect as a facile and versatile electrolyte strategy. Kosmotropic/chaotropic anions play a viable role in manipulating ion coordination structures and intermolecular interactions of electrolyte couples involved in the BLE, thus enabling customized control of their miscibility/immiscibility. As a proof-of-concept, rechargeable zinc (Zn)-metal batteries are selected owing to naturally abundant/low-cost Zn with a high theoretical capacity (820 mA h g_{Zn}^{-1}), safety, and simple cell fabrication.[18] Conventional Zn-metal batteries use aqueous or organic electrolytes; however, this single-phase electrolyte fails to simultaneously fulfill the heterogeneous requirements of anodes and cathodes. To resolve this longstanding problem, we prepare a BLE by coupling a cathode-customized aqueous electrolyte (3.4 m zinc sulfate ($ZnSO_4$) in water, m represents molality [mol kg^{-1}]) and an anode-customized nonaqueous electrolyte (0.5 m zinc bis(trifluoromethanesulfonyl)imide ($Zn(TFSI)_2$) in acetonitrile (AN)).

The key underlying technology for the BLE is the phase separation of its electrolyte couples using a principle of ''demixing the miscible liquids''. Despite the intrinsic miscibility of water (in the aqueous electrolyte) and AN (in the nonaqueous electrolyte), the structural change of the aqueous electrolyte induced by kosmotropic SO_4^{2-} allows the demixing (*i.e.*, phase separation) with the nonaqueous electrolytes. The resulting BLE exhibits an exceptionally high ionic conductivity (37.0 mS cm^{-1} at 25 °C), which far exceeds those of previously reported biphasic electrolytes. The phase-separated, aqueous and nonaqueous electrolytes in the BLE facilitate redox kinetics at $CaV_6O_{16}{\cdot}3H_2O$ (CVO) cathodes and Zn plating/stripping reversibility at Zn anodes. Driven by this electrode-customized electrochemical viability and high ionic conductivity of the BLE, a Zn‖CVO full cell exhibits a high specific capacity (299 mA h g_{CVO}^{-1}) and a long cyclability (86.6% retention after 3500 cycles). Moreover, the BLE enables a Zn anode-free full cell to exhibit a high energy density (183 W h kg^{-1}) along with a stable capacity retention (76.7% after 100 cycles), which lie beyond those achievable with previously reported Zn batteries.

Results and discussion

Effects of kosmotropic/chaotropic anions on the electrolyte structure

We investigated the effects of kosmotropic/chaotropic anions on the electrolyte structure, with a focus on the intermolecular interactions between the aqueous and nonaqueous electrolytes. The water structure in aqueous electrolytes, which refers to the degree of intermolecular interactions, local packing, and orientation of water molecules and their surroundings, is described in terms of chaotropes (Greek meaning ''disorder'') or kosmotropes (Greek meaning ''order'') in the Hofmeister series.[19,20] The chaotropes (structure-breaker), which are large ions with low charge density, show weaker interactions with water compared to those of water molecules themselves, thereby disrupting the water structure. In contrast, small ions with high charge density are classified as kosmotropes (structure-maker), which favor the development of structured water with reduced free water. It is known that the water structure is more affected by anions than cations.[21]

The structural change of water in aqueous electrolytes was theoretically investigated by varying anion species (*e.g.*, $TFSI^-$, trifluoromethanesulfonate (OTf^-), chloride (Cl^-), acetate (OAc^-), and SO_4^{2-}). Electrostatic potential (ESP) values of the anions, which are used as an indicator representing their affinity with water, were evaluated using density functional theory (DFT) calculations (Fig. 1a). Water can interact preferentially with anions having more negative ESP values. The ESP values of the anions are decreased in this order: $TFSI^- > OTf^- > Cl^- > OAc^- > SO_4^{2-}$. This tendency was verified by the results of water–anion interaction energy, H-bond numbers, H-bond distance (Fig. S1, ESI†), and hydration structure of anions (Fig. S2, ESI†). $TFSI^-$, which is known as a strong chaotropic anion, showed the weakest interaction with water. The opposite behavior was observed at SO_4^{2-}, which was the strongest kosmotropic anion examined herein.

The structural state of the aqueous electrolytes was investigated as a function of anion species and salt concentration using the Fourier-transform infrared spectroscopy (FTIR) analysis (Fig. 1b). The O–H stretching (3000–3700 cm^{-1}) vibrational band of water is often deconvoluted into three Gaussian components, depending on the strength of the intermolecular force (IMF) between water and environment (*e.g.*, weak IMF at ~3600 cm^{-1}, moderate IMF at ~3400 cm^{-1}, and strong IMF at ~3200 cm^{-1}).[22] As the chaotropic effect was intensified in the order of 0.5 m $Zn(OTf)_2$, 0.5 m $Zn(TFSI)_2$, and 1.0 m $Zn(TFSI)_2$, the FTIR spectra showed lower absorbance of strong/moderate IMF and higher absorbance of weak IMF compared to the results of pure water, indicating that the chaotropic effect can hinder the water structuring in the

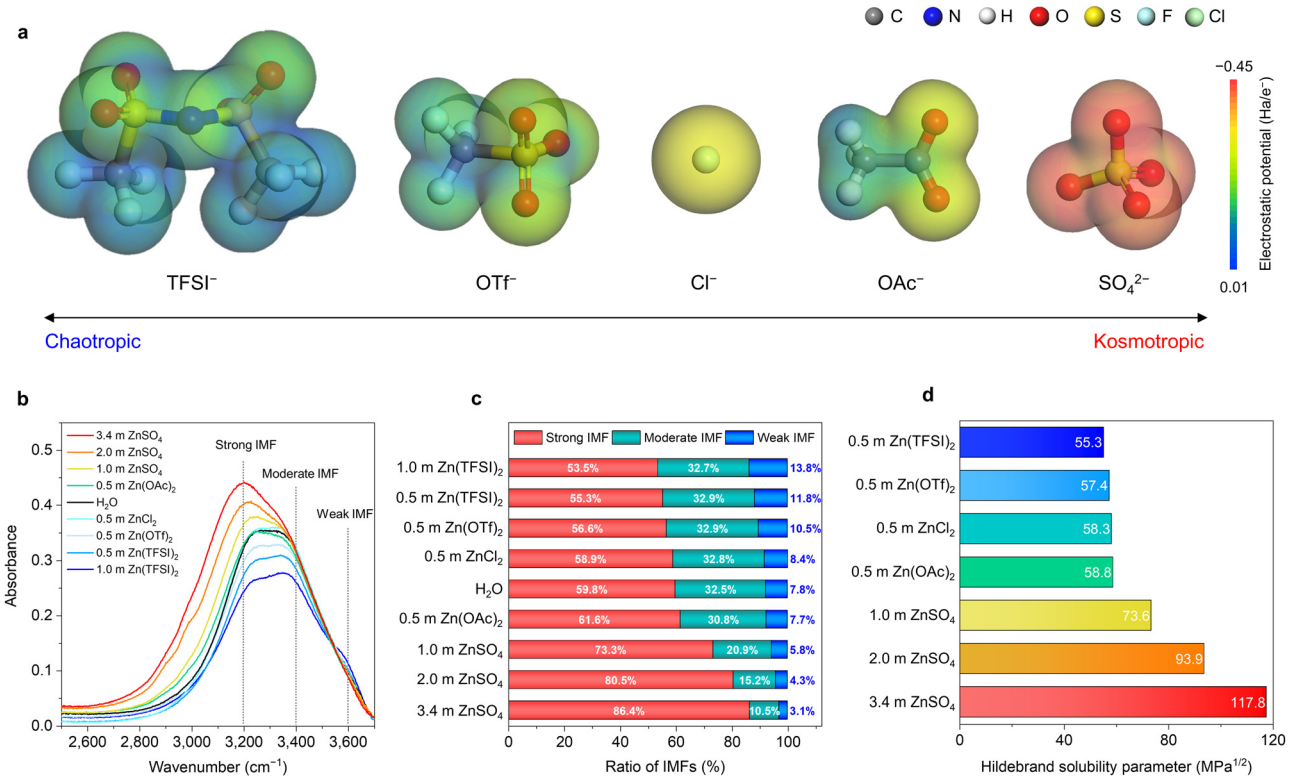

Fig. 1 Effects of kosmotropic/chaotropic anions on electrolyte structure. (a) Schematic depicting electrostatic potential values of anions ($TFSI^-$, OTf^-, Cl^-, OAc^-, and SO_4^{2-}) which are used as an indicator representing their affinity with water. Gray, blue, white, red, yellow, cyan, and light green balls represent carbon, nitrogen, hydrogen, oxygen, sulfur, fluorine, and chlorine respectively. (b) FTIR spectra of various aqueous electrolytes as a function of anion species and salt concentration under the same anion concentration. (c) Comparison in the relative portion of the three (strong, moderate, and weak) IMFs obtained from O–H stretching bands in the FTIR spectra. (d) Hildebrand solubility parameter (δ) values of the electrolytes calculated from the MD trajectory.

electrolytes. In contrast, as the kosmotropic effect increased in the order of 0.5 m $Zn(OAc)_2$, 1.0 m $ZnSO_4$, 2.0 m $ZnSO_4$, and 3.4 m $ZnSO_4$, the FTIR spectra showed higher absorbance of strong IMF and lower absorbance of weak IMF than those of pure water, revealing that the kosmotropic anions are strongly hydrated owing to their structure-making ability. Meanwhile, the intermediate Cl^- negligibly affected the structural state of water. These tendencies were quantitatively confirmed by analyzing the relative portion of three IMFs in the O–H stretching bands (Fig. 1c and Fig. S3, ESI†). As additional evidence, the Hildebrand solubility parameter (δ) values of the electrolytes were estimated by calculating the molecular dynamics (MD) trajectory (Fig. 1d and Table S1, ESI†). The electrolytes with kosmotropes showed higher δ values than those with chaotropes at a fixed anion concentration. In addition, the δ value was increased with increasing the $ZnSO_4$ concentration. To confirm the effects of kosmotropic/chaotropic anions on electrolyte structure, the comparison between the aforementioned different anions was repeated at a low salt concentration of 0.5 m (Fig. S4, ESI†). These results demonstrate the chemical viability of kosmotropic/chaotropic anions in controlling intermolecular interactions, eventually affecting the water structure of the aqueous electrolytes.

Relationship between electrolyte structure and phase separation

The structure change of the aqueous electrolytes described above could affect phase separation with nonaqueous solvents. Diethyl ether (DEE), which is intrinsically immiscible with water, was coupled with various aqueous electrolytes (Fig. S5 and Table S2, ESI†). Notably, DEE was miscible with 1.0 m $Zn(TFSI)_2$ aqueous electrolyte having a disordered water structure, playing the role of strong chaotropic $TFSI^-$. This result was verified by examining the interaction energy (ΔE_{int}) between aqueous electrolytes and DEE through MD simulations (Fig. S6, ESI†). The more-developed chaotropic anions in the disordered aqueous electrolytes showed a stronger ΔE_{int} with DEE due to the weakened water–water interactions, indicating the facilitated mixing with DEE.

As an opposite case, AN, which shows good miscibility with water, was coupled with various aqueous electrolytes (Fig. 2a). 1.0 m $Zn(TFSI)_2$ aqueous electrolyte was miscible with AN due to the weakened water–water interactions by strong chaotropic $TFSI^-$. In addition, 0.5 m $Zn(OAc)_2$ aqueous electrolyte was miscible with AN, indicating insufficient structure-making ability by OAc^-. By comparison, ordered aqueous electrolytes having kosmotropic SO_4^{2-} were phase-separated from AN. Positions of AN-aqueous electrolyte interfaces gradually shifted upwards with increasing salt ($ZnSO_4$) concentration from 1.0 to 3.4 m. This result was theoretically verified using the MD simulation (Fig. 2b). AN was mixed with aqueous electrolytes having the disordered and insufficiently ordered structures (1.0 m $Zn(TFSI)_2$ and 0.5 m $Zn(OAc)_2$). By comparison, the

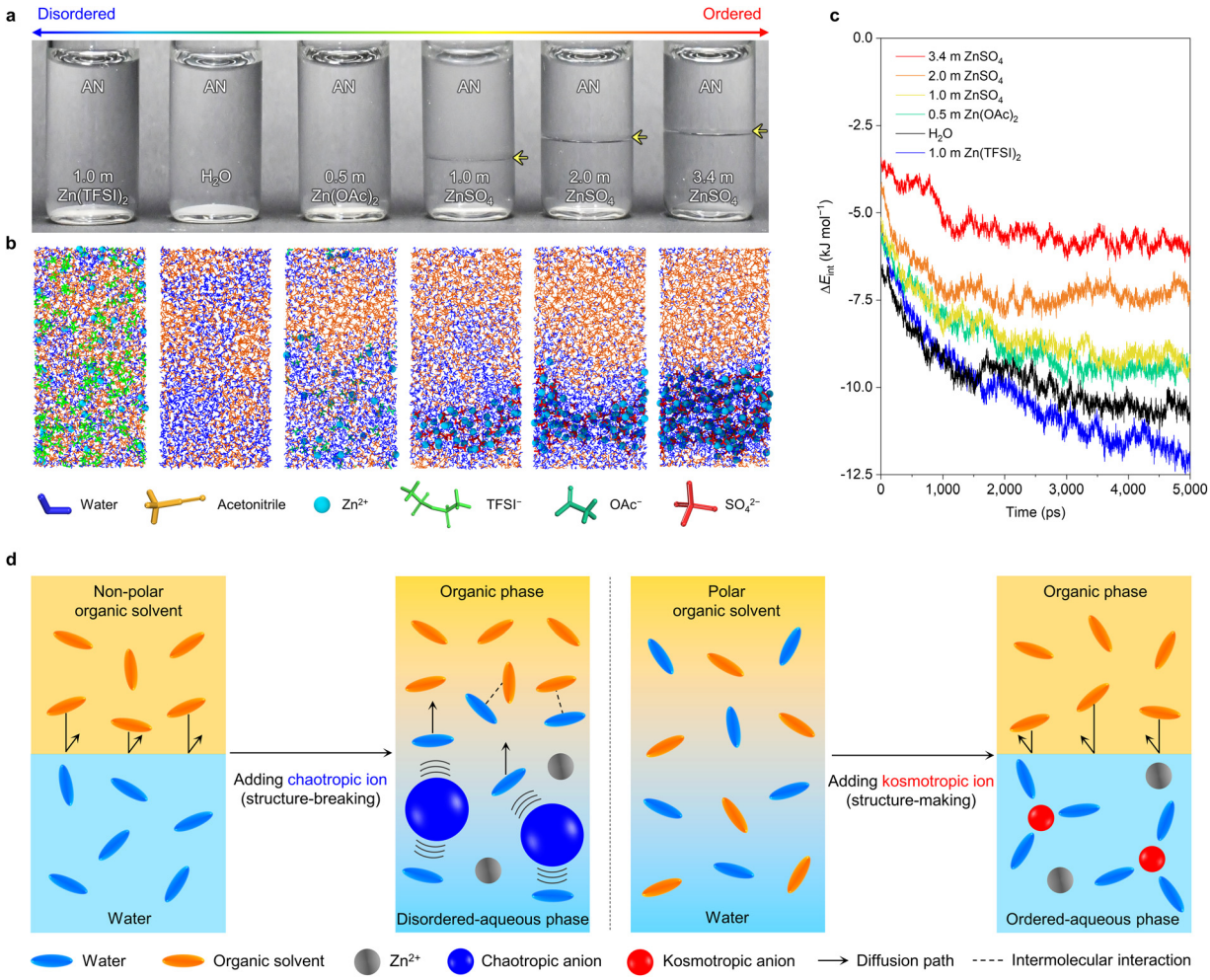

Fig. 2 Relationship between electrolyte structure and phase separation. (a) Photograph of various aqueous electrolyte/AN (1/1, v/v) mixtures at ambient temperature. (b) Snapshots of various aqueous electrolyte/AN (1/1, v/v) mixtures after 5 ns of MD simulation. H_2O, AN, Zn^{2+}, $TFSI^-$, OAc^-, and SO_4^{2-} molecules are depicted as blue, orange, cyan, green, teal, and red colors, respectively. (c) Time evolution of the interaction energy (ΔE_{int}) between water (in the aqueous electrolytes) and AN, in which ΔE_{int} is normalized by the number of water molecules. (d) Schematic depicting the structural change of aqueous electrolytes induced by the chaotropic/kosmotropic effects and its influence on the miscibility/immiscibility with nonaqueous solvents.

$ZnSO_4$ aqueous electrolytes tended to segregate from AN-rich phases because the kosmotropic SO_4^{2-} tightly holds water molecules. By increasing the $ZnSO_4$ concentration to 3.4 m, the amount of water bound to SO_4^{2-} considerably increased, thus promoting the phase separation with AN. To theoretically interpret this phase separation behavior, ΔE_{int} between water (in the aqueous electrolytes) and AN was calculated (Fig. 2c) and discussed in terms of its relative comparison between the target mixtures. With respect to ΔE_{int} (−10.6 kJ mol^{-1}) for the pure water–AN mixture, an aqueous electrolyte of 1 m $Zn(TFSI)_2$ showed a slightly larger negative ΔE_{int} (−11.9 kJ mol^{-1}), indicating the enhanced intermolecular interaction between AN and water. In contrast, the absolute values of ΔE_{int} were smaller as the kosmotropic effect became stronger (0.5 m $Zn(OAc)_2$: −9.4 kJ mol^{-1}, 1.0 m $ZnSO_4$: −9.1 kJ mol^{-1}, and 3.4 m $ZnSO_4$: −5.9 kJ mol^{-1}). This result exhibits the viable role of kosmotropic SO_4^{2-} in enabling the phase separation with AN that is intrinsically miscible with pure water. The universality of kosmotropic/chaotropic anions-driven phase separation control was further explored: dimethyl carbonate (DMC) and ethyl acetate (EA) as water-immiscible solvents (Fig. S7, ESI†), and trimethyl phosphate (TEP), diglyme (G2), and propylene carbonate (PC) as water-miscible solvents (Fig. S8, ESI†).

The structural change of aqueous electrolytes induced by the kosmotropic/chaotropic anions and its influence on the miscibility/immiscibility with nonaqueous solvents are schematically depicted in Fig. 2d. Chaotropic anions disturb intermolecular interactions in aqueous electrolytes, thus rendering the water structure disordered. As a result, the interaction energy between water in the disordered structure and nonaqueous solvents could be enhanced, eventually promoting their miscibility.[23,24] In contrast, kosmotropic anions are strongly hydrated, contributing to ordering the water structure in aqueous electrolytes. Consequently, interaction energies between water and nonaqueous solvents become weakened, resulting in phase separation even with polar solvents. Manipulating ion coordination structures and intermolecular interactions of liquid couples through kosmotropic/chaotropic anions can be suggested as a versatile technology

platform to enable customized control of their miscibility/immiscibility.

Biphasic liquid electrolytes for Zn-metal full cells

A challenge facing rechargeable Zn-metal full cells is the absence of suitable electrolytes that can simultaneously fulfill the heterogeneous chemical/electrochemical requirements of anodes and cathodes. Aqueous electrolytes allow fast Zn^{2+} redox kinetics at cathodes,[25] however, they undergo vigorous interfacial side reactions with Zn metal anodes. On the other hand, non-aqueous electrolytes tend to display good chemical/electrochemical stability toward Zn metal anodes.[26] However, sluggish electrochemical reactions at cathode–electrolyte interfaces often cause poor rate performance.[25]

To address this challenging issue, we designed the BLE based on a cathode-customized aqueous electrolyte and a Zn anode-customized organic electrolyte. As a cathode-customized electrolyte, 3.4 m $ZnSO_4$ aqueous electrolyte (denoted as "AE") was chosen to allow fast reaction kinetics at cathodes and phase separation with anode-customized electrolytes. Meanwhile, an organic electrolyte comprising AN and $Zn(TFSI)_2$ was prepared for Zn metal anodes to achieve chemical stability/electrochemical reversibility with Zn metals and high ionic conductivity. An optimum $Zn(TFSI)_2$ concentration of the organic electrolytes was determined to be 0.5 m by considering both their ionic conductivity (Fig. S9, ESI†) and phase separation with the AE (Fig. S10, ESI†). Eventually, 0.5 m $Zn(TFSI)_2$ in AN ("OE", as an anode-customized organic electrolyte) was combined with the AE to produce the BLE (Fig. 3a).

The phase separation behavior of the BLE was investigated. The Raman spectra (Fig. 3b) showed that characteristic peaks of water (3234 and 3412 cm^{-1}) and SO_4^{2-} (985 cm^{-1})[27] were observed exclusively at the bottom layer of the BLE, whereas the peaks of AN (917, 2253, and 2289 cm^{-1})[28] and $TFSI^-$ (742 cm^{-1})[29] were detected at the top layer. This phase separation of the BLE was further elucidated by comparing the Hildebrand solubility parameter (δ) of the solvents and electrolytes (Fig. 3c). From the principle of "like dissolves like", two different systems tend to be immiscible when they have larger $\Delta\delta$.[30] For the solvent mixture of water and AN, $\Delta\delta$ (δ (water) – δ (AN)) was 21.8 $MPa^{1/2}$. By comparison, the electrolyte mixture showed larger $\Delta\delta$ (δ (3.4 m $ZnSO_4$ in water) – δ (0.5 m $Zn(TFSI)_2$ in AN))

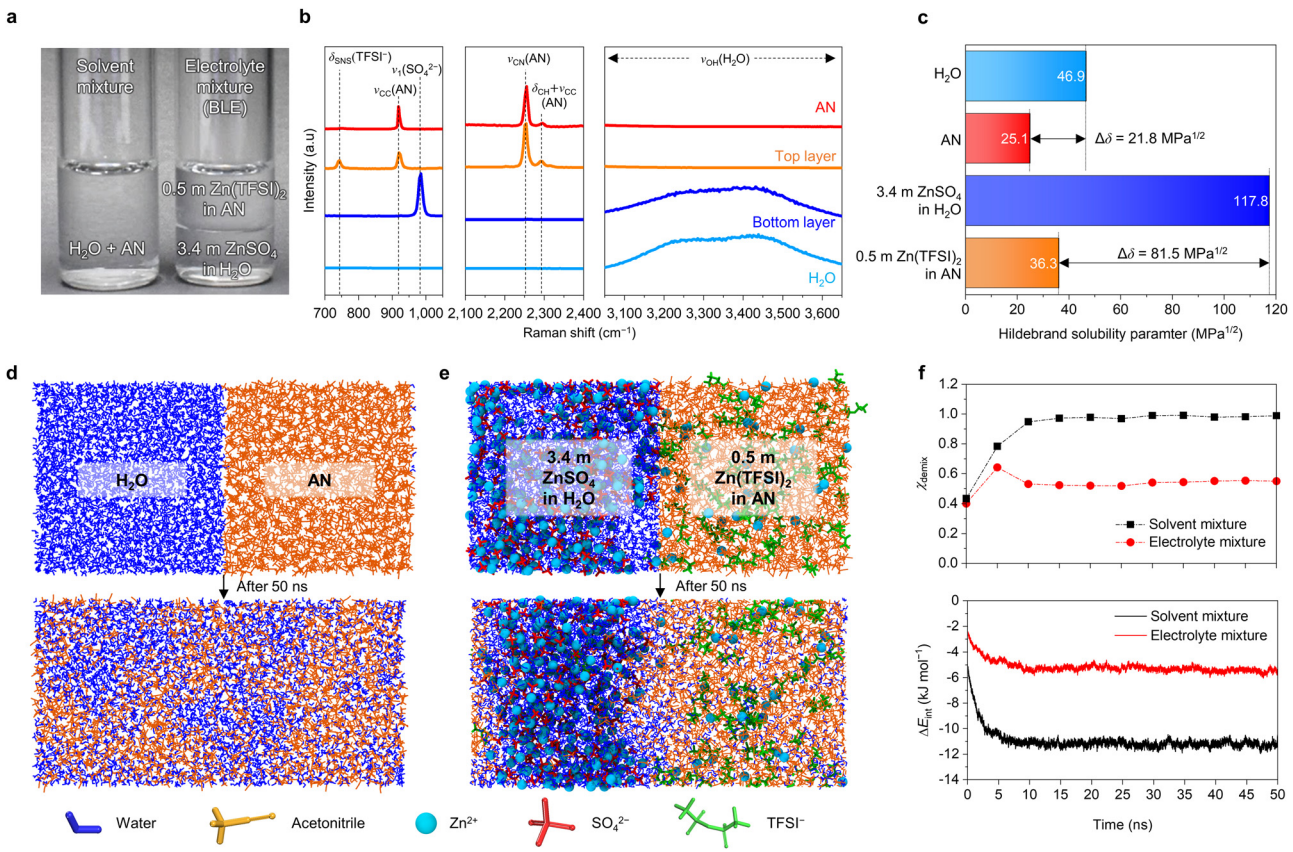

Fig. 3 Biphasic liquid electrolytes for Zn-metal full cells. (a) Photographs of the miscible solvent mixture (water/AN = 1/1 (v/v)) and immiscible electrolyte mixture (3.4 m $ZnSO_4$ in water/0.5 m $Zn(TFSI)_2$ in AN = 1/1 (v/v)). (b) Raman spectra of the top/bottom layers in the BLE along with solvents (water and AN). Raman vibrational modes are denoted as follows: C–C stretching (ν_{CC}), C N stretching (ν_{CN}), C–H bending (δ_{CH}), O–H stretching (ν_{OH}), symmetric stretching mode of SO_4^{2-} ($\nu_1(SO_4^{2-})$), and S–N–S bending mode of $TFSI^-$ ($\delta_{SNS}(TFSI^-)$). (c) Hildebrand solubility parameter (δ) values of the solvents and electrolytes. $\Delta\delta$ denotes the difference in the solubility parameter between the two components. MD simulations describing the (d) miscible solvent mixture and (e) immiscible electrolyte mixture. H_2O, AN, Zn^{2+}, SO_4^{2-}, and $TFSI^-$ molecules are depicted as blue, orange, cyan, red, and green colors, respectively. (f) Time evolution of the demixing index (χ_{demix}) and the interaction energy (ΔE_{int}) of the solvent and electrolyte mixtures, in which ΔE_{int} is normalized by the number of water molecules.

of 81.5 $MPa^{1/2}$, exhibiting the thermodynamic phase separation. Furthermore, MD simulations were conducted to elucidate the molecular states of the solvent and electrolyte mixtures (Table S3, ESI†). The solvent mixture became homogeneous just after a mixing time of 50 ns (Fig. 3d), whereas the electrolyte mixture maintained the phase separation (Fig. 3e). This difference in the phase separation was quantified by calculating the demixing index (χ_{demix}) and ΔE_{int} as a function of the elapsed time (Fig. 3f). χ_{demix} of the solvent mixture promptly reached 1 (complete miscibility) after a mixing time of 10 ns, whereas the electrolyte mixture maintained low χ_{demix} (immiscibility). Moreover, ΔE_{int} of the electrolyte mixture was lower than that of the solvent mixture, verifying the kosmotropic effect-driven phase separation of the BLE. Meanwhile, the AE and OE in the BLE stably maintained the phase separation even after vigorous shaking (Video S1, ESI†), indicating the potential use of the BLE in various operating conditions.

Ion transport phenomena

The ionic conductivity of the BLE was compared with those of previously reported biphasic electrolytes (Fig. 4a, Fig. S11, and Table S4, ESI†). Most of the biphasic electrolytes have suffered

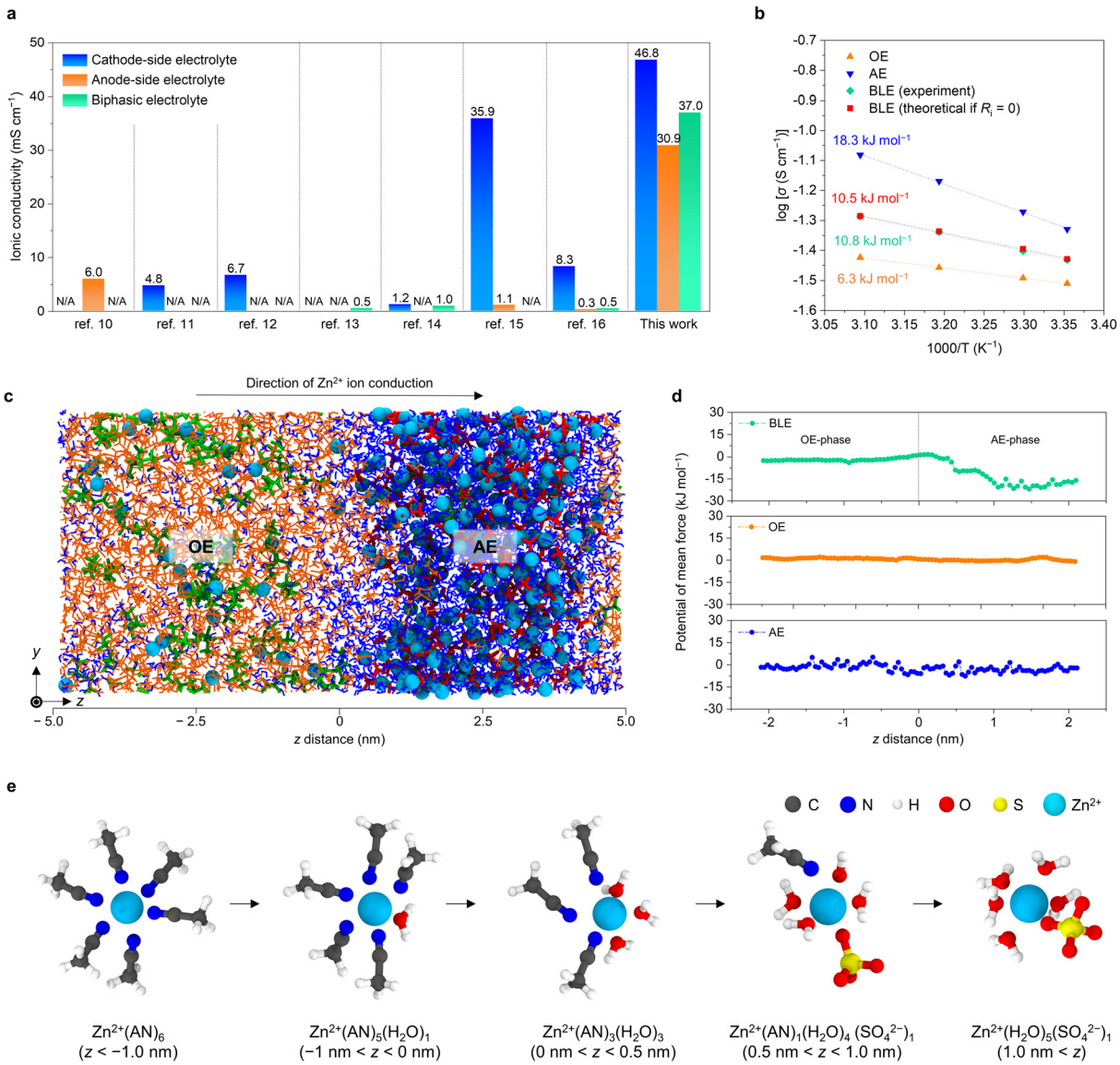

Fig. 4 Ion transport phenomena. (a) Comparison in ionic conductivities between the BLE (including its electrolyte couples (AE and OE)) and previously reported biphasic electrolytes. N/A (not available) indicates no experimental data in the references. (b) Temperature-dependent ionic conductivities of the BLE, its electrolyte couples (AE and OE), and theoretical ionic conductivities were calculated based on the assumption of neglecting OE–AE interfacial resistance. (c) MD simulation depicting the ion transport phenomena in the BLE with a focus on the OE/AE phases and OE–AE interface. H_2O, AN, Zn^{2+}, SO_4^{2-}, and $TFSI^-$ molecules are depicted as blue, orange, cyan, red, and green colors, respectively. (d) Potential of mean force (PMF) profiles of Zn^{2+}. Starting configurations for the PMF sampling simulation were generated by placing a representative Zn^{2+} solvation shell from the reference point along the z-axis, with a sampling window of 0.2 nm. (e) Snapshots depicting the change in the first solvation shell of Zn^{2+} at OE-rich region ($z < -1.0$ nm), interface region (-1.0 nm $< z <$ 1.0 nm) and AE-rich region ($z >$ 1.0 nm).

from low ionic conductivity because of a large gap in the ion conduction capability between their two electrolyte constituents containing solvent pairs with opposite polarities.[10 16] Specifically describing, a nonpolar solvent-containing electrolyte constituent in the biphasic electrolyte tended to show low ionic conductivity due to the insufficient dissociation capability of the nonpolar solvent, whereas the other electrolyte constituent with a polar solvent could provide decent ionic conductivity. In contrast, the two electrolyte couples in the BLE contained the polar solvent pairs (*i.e.*, acetonitrile and water), thus beneficially contributing to high ionic conductivity. We note that manipulating the ion coordination structures and intermolecular interactions of the electrolyte couples (based on the miscible polar solvent pairs of acetonitrile and water) enabled their phase separation, while simultaneously achieving the high ionic conductivity of the BLE. As result, the BLE showed higher ionic conductivity (σ) of 37.0 mS cm^{-1} at 25 °C due to two major contributions: (1) high ionic conductivities of its electrolyte couples based on polar solvent pairs, *i.e.*, AE (σ = 46.8 mS cm^{-1} at 25 °C) and OE (σ = 30.9 mS cm^{-1} at 25 °C) and (2) negligibly low energy barrier for ion conduction across the OE–AE interface.

The ion conductivity and activation energy (E_a) for ion conduction of the BLE were positioned between those of AE and OE (Fig. 4b). Moreover, the experimental ionic conductivity of the BLE appeared similar to the theoretical ionic conductivity which neglected OE–AE interfacial resistance (detailed information for the calculation is provided in the Fig. S12 and Table S5, ESI†). This result indicates that the resistance at the OE–AE interface may be negligibly small, thereby minimally impairing the ion conduction of the BLE.

The ion transport phenomena in the BLE were investigated using MD simulation (Fig. 4c). The potential of mean force (PMF) of Zn^{2+} was calculated to investigate the energy barrier of ion conduction in the BLE and its electrolyte couples (Fig. 4d). The pristine OE showed a smooth and flat profile at PMF of $\sim$2.5 kJ mol^{-1}. Meanwhile, a larger fluctuation of the PMF profile was observed in the pristine AE, which is attributed to a strong interaction with neighboring concentrated ions. For the BLE, the PMF profile was flat in the OE phase and fluctuated while moving into the AE phase, which appeared similar to those of the pristine OE and AE, respectively, exhibiting the phase separation between the OE and AE phases. In addition, the PMF at the OE–AE interface showed minor fluctuation, indicating that the ion conduction across the interface is not sluggish.

The change in the solvation structure of Zn^{2+} across the OE–AE interface was traced under an electric field of 0.5 V nm^{-1} that acts as a driving force for ion migration (Fig. 4e). In the OE phase ($z < -1$ nm), Zn^{2+} is solvated with AN to form a solvated complex of $Zn^{2+}(AN)_6$. As the solvated Zn^{2+} moves toward the OE–AE interfacial region (-1 nm $< z <$ 1 nm), desolvation of AN and subsequent solvation of water continuously occur. The ratio of water in the solvation sheath increases while Zn^{2+} further migrates into the AE phase. Eventually, Zn^{2+} is completely solvated by water and sulfate ions in the AE phase (1 nm $< z$). This result demonstrates that the BLE undergoes stepwise desolvation/solvation while maintaining the phase separation between the OE and AE phases.

Electrode-customized electrochemical characteristics

The effects of the electrolyte couples (OE and AE) in the BLE on the electrochemical performances of anodes and cathodes were investigated. The OE showed a lower static contact angle (26.6°) on the Zn metal compared to that (90.6°) of the AE (Fig. S13, ESI†), revealing the superior wettability that can beneficially affect Zn plating/stripping reversibility.[31] In addition, the Zn metal remained almost intact after being soaked in the OE (Fig. S14, ESI†) and did not generate any gas bubbles in the OE during Zn plating/stripping cycling (Fig. S15, ESI†), exhibiting the chemical/electrochemical stability of the OE against the Zn metal. Moreover, the Tafel plots revealed that the OE showed a significantly lower Zn corrosion current density than the AE (Fig. S16, ESI†). These results verify the high anti-corrosion property of the OE against the Zn metal.

The coulombic efficiency (CE) of Zn plating/stripping was measured using a Zn‖Ti cell (Fig. 5a and S17, ESI†). The cell employing the OE showed a high CE of 99.6% after 300 cycles, in comparison to a cell with the AE that failed to operate after 63 cycles. This advantageous effect of the OE on Zn metals was verified by long-term cycling of Zn‖Zn symmetric cells (Fig. 5b). The cell with the OE showed stable cycling performance over 800 h owing to high chemical/electrochemical stability toward Zn metal electrodes, despite the slightly larger voltage hysteresis which often arises from the relatively high Zn^{2+} desolvation energy[25] and low ionic conductivity[32] of nonaqueous electrolytes. In contrast, the cell with the AE showed a sudden failure of cycling just after 100 h. Moreover, such superior cyclability of the cell with the OE was also observed at higher areal current density (1.5 mA cm^{-2}) and areal capacity (1 mA h cm^{-2}) (Fig. S18, ESI†). This stable Zn plating/stripping cyclability with the OE was elucidated by electrochemical/structural analysis of the cycled Zn electrodes without Zn dendrites (Fig. S19, S20, and S21, ESI†) and Zn corrosion (Fig. S22, ESI†).

As a cathode material for Zn-metal batteries, CVO, which has a layered structure suitable for reversible Zn^{2+} insertion/extraction, was synthesized according to the previous study[33] and its structure was analyzed by X-ray diffraction (XRD) (Fig. S23, ESI†) and scanning electron microscopy (SEM) (Fig. S24, ESI†). To examine the compatibility of the CVO toward the AE (or OE), EIS analysis of pre-zincificated CVO (Zn_xCVO, 50% depth of discharge (DOD)) symmetric cells was conducted in the temperature range of 25–50 °C (Fig. S25, ESI†). The cell with the AE showed lower charge transfer resistance (R_{ct}) and E_a for charge transfer reaction compared to that of the OE (Fig. 5c). This result demonstrates that the AE can facilitate interfacial charge transfer reaction at CVO cathode, which is mainly attributed to a low energy barrier of Zn^{2+} desolvation in aqueous electrolytes.[25]

Galvanostatic intermittent titration technique (GITT) analysis of a Zn‖CVO cell with the AE showed a substantial decrease in the polarization during the repeated current stimuli compared to the cell with the OE (Fig. 5d). From the GITT profiles,

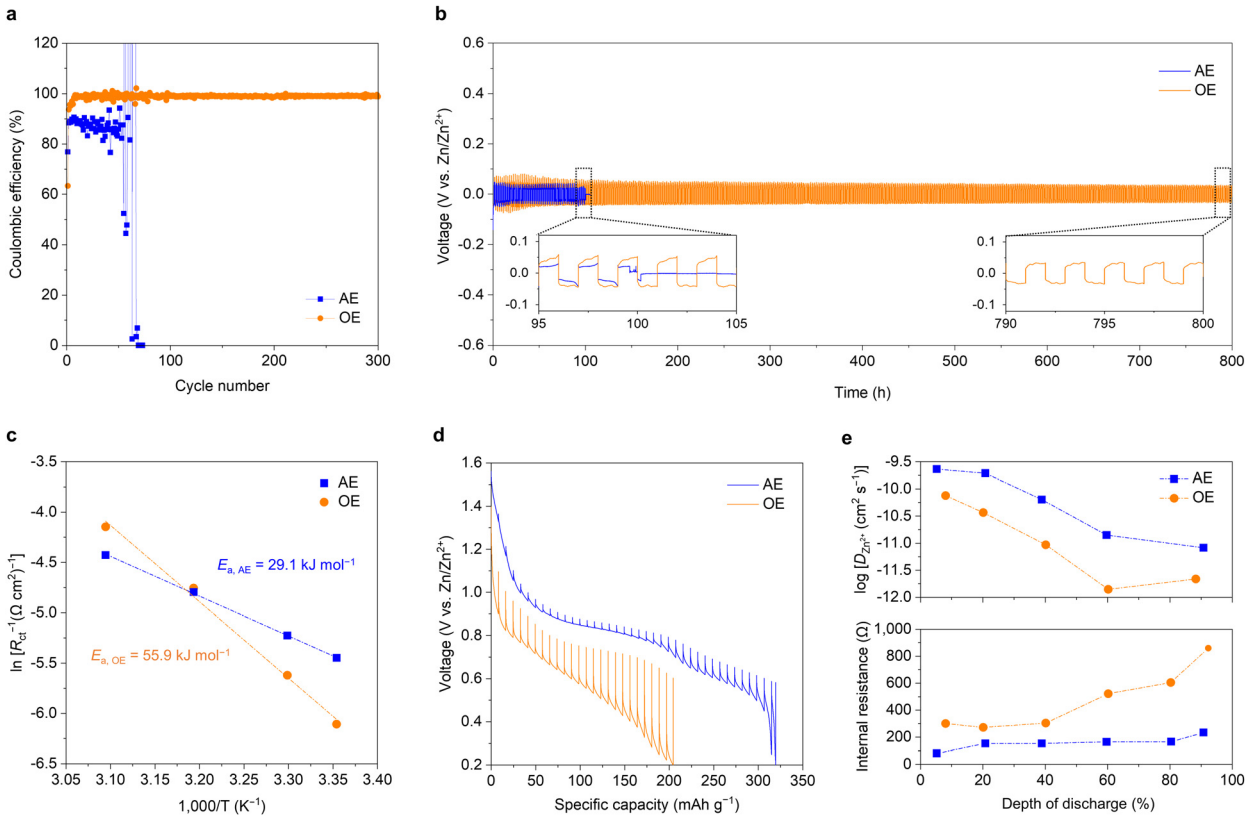

Fig. 5 Electrode-customized electrochemical characteristics. (a) CE of Zn plating/stripping using Zn‖Ti cells with AE and OE at a current density of 0.1 mA cm^{-2} and an areal capacity of 0.1 mA h cm^{-2}. (b) Voltage profiles of Zn‖Zn symmetric cells with AE and OE at a current density of 0.1 mA cm^{-2} and an areal capacity of 0.1 mA h cm^{-2}. (c) The activation energy (E_a) for charge transfer reaction of pre-zincificated Zn_xCVO (50% DOD) symmetric cells with AE and OE. (d) GITT profiles of Zn‖CVO cells with AE and OE at a current density of 100 mA g^{-1} and interruption time between each pulse of 1 h. (e) Change in Zn^{2+} diffusion coefficients ($D_{Zn^{2+}}$) and internal resistance as a function of DOD, which was calculated from the GITT profiles.

the corresponding Zn^{2+} diffusion coefficients ($D_{Zn^{2+}}$) into the CVO cathode and internal resistance were calculated as a function of DOD (see Table S6 in the ESI† for calculation details). The cell with the AE presented higher $D_{Zn^{2+}}$ and lower internal resistance than the cell with the OE (Fig. 5e), verifying that the AE can facilitate Zn^{2+} diffusion kinetics at the cathode–electrolyte interface. In addition, cyclic voltammetry (CV) profiles of the Zn‖CVO cells showed that the AE facilitates the multi-step process of Zn^{2+} insertion/extraction with diffusion-controlled behavior[34] compared to the OE (Fig. S26, ESI†). The above-described results demonstrate that the AE can promote both Zn^{2+} diffusion and charge transfer reaction kinetics, underscoring its beneficial contribution as a CVO-customized electrolyte.

Application to Zn-metal full cells

Application of the BLE to Zn-metal full cells was investigated. The CV profiles of a Zn‖CVO cell with the BLE showed two pairs of characteristic redox peaks assigned to the multi-step process of Zn^{2+} insertion/extraction (Fig. S27, ESI†). In addition, the Zn‖CVO cell showed a specific capacity of 299 mA h g^{-1} and stable charge/discharge profiles even at 1000 mA g^{-1} (Fig. S28, ESI†). This fast rate performance of the cell with the BLE was comparable to that of the AE (Fig. S29, ESI†), whereas the poor rate performance was observed at the OE, exhibiting that Zn^{2+} insertion/extraction kinetics at the CVO cathode governs the rate capability of the cell.

The cycling performance of the Zn‖CVO cell was examined (Fig. 6a and S30, ESI†). The cell with the OE presented a discharge capacity of only 76 mA h g^{-1} in the 1st cycle at a current density of 500 mA g^{-1} because of sluggish reaction kinetics at the CVO cathode. Furthermore, the cell with the OE suffered from severe capacity decay with cycling, which is mainly attributed to the structural instability[35] of the CVO in contact with the OE (Fig. S31, ESI†). Meanwhile, the cell with the AE showed high specific capacities during initial cycles. However, the capacity with cycling continuously decreased due to water-triggered unwanted side reactions and Zn dendrite growth. In contrast, the cell with the BLE showed a high initial capacity of 160 mA h g^{-1} and a stable cyclability (86.6% retention after 3500 cycles), which exceeded those of 2.0 M (~2.0 m) $ZnSO_4$ aqueous electrolyte that is commonly used in Zn-metal batteries.[18] This superior cycling performance of the Zn‖CVO cell with the BLE was verified by analyzing the EIS profiles after 3500 cycles (Fig. S32, ESI†) and conducting post-mortem analysis of the cycled Zn anodes with a focus on surface morphology and distribution of oxidized species (Fig. S33 and S34, ESI†). The long-term cyclability of the BLE was attributed to the combined effect of the AE (enabling facile

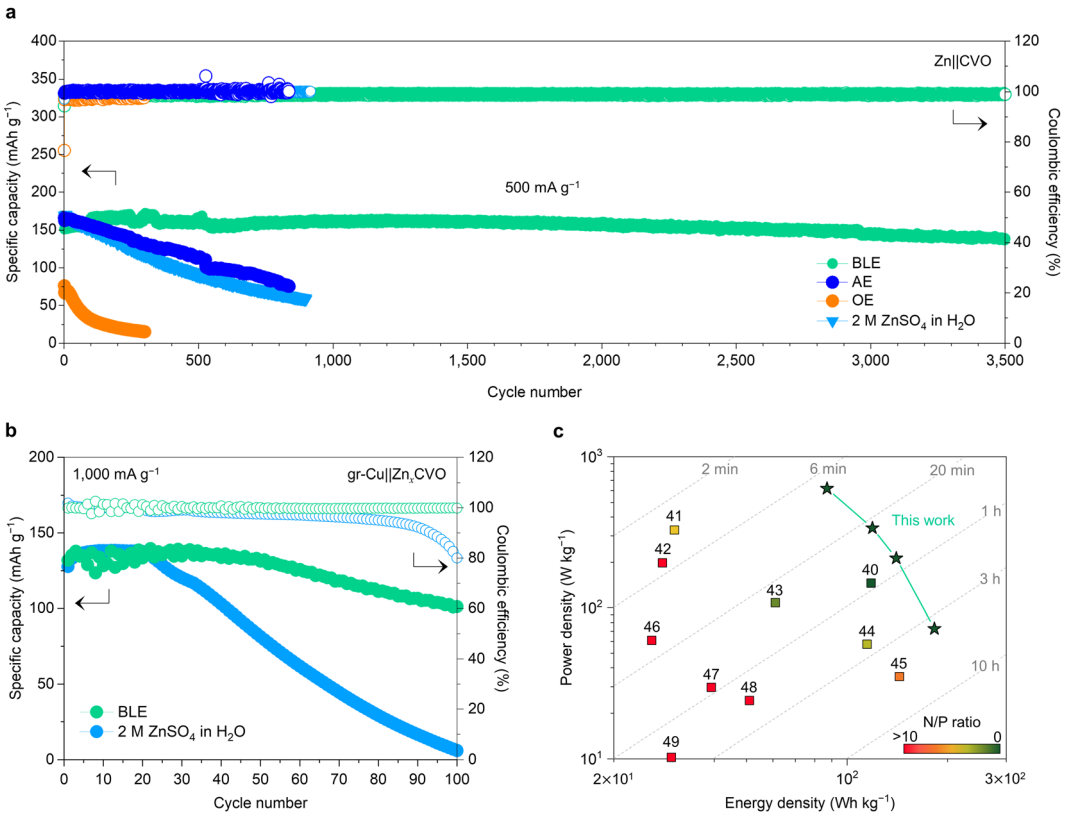

Fig. 6 Application to Zn-metal full cells. (a) Galvanostatic cycling performance of Zn||CVO full cells with AE, OE, 2 M $ZnSO_4$ aqueous electrolyte, and BLE at a current density of 500 mA g^{-1}. (b) Galvanostatic cycling performance of Zn anode-free full cells with 2 M $ZnSO_4$ aqueous electrolyte and BLE at a current density of 1000 mA g^{-1}. (c) Ragone plot showing energy and power densities (estimated based on the total weight of electrode active materials) of this study and previously reported Zn batteries in terms of negative/positive electrode capacity ratio (N/P ratio).

reaction kinetics at the CVO cathode) and the OE (contributing to high reversibility and thermodynamic stability with the Zn anode).

Stimulated by the electrode-customized viability and high ionic conductivity of the BLE, its application to a Zn anode-free full cell, which has zero-excess Zn,[36,37] was explored. Despite the benefit in cell-energy-density, the practical use of the Zn anode-free configuration has been plagued by poor cyclability. The Zn anode-free cell was fabricated using a Zn_xCVO cathode and a Cu foil modified with a graphene monolayer (gr-Cu)[38] which showed high Zn^{2+} reversibility compared to other current collectors (Fig. S35, ESI†). The cell with conventional 2.0 M $ZnSO_4$ aqueous electrolyte showed low cycling retention because of irreversible Zn consumption (Fig. 6b and S36, ESI†). In contrast, the cell with the BLE exhibited a higher capacity retention of 76.7% after 100 cycles and a faster rate capability (141 mA h g^{-1} at 1000 mA g^{-1}) (Fig. S37, ESI†), which lie beyond those achievable with previously reported anode-free cells (Table S7, ESI†). The capacity fluctuation in the initial cycles could be due to the activation process of the CVO cathode in contact with the AE (*i.e.*, 3.4 m $ZnSO_4$ in H_2O), which is often observed for vanadium-based cathodes with high-concentration aqueous electrolytes.[39] More notably, the specific energy/power densities of the anode-free full cell with the BLE (183/73–87/618 [W h kg^{-1}/W kg^{-1}], estimated based on the total weight of electrode active materials) far exceeded the results of previously reported Zn batteries (Fig. 6c and Table S8, ESI†).[40 49]

Conclusions

In summary, we presented a biphasic liquid electrolyte (BLE) based on the kosmotropic effect as a new electrolyte strategy to fulfill the heterogeneous chemical/electrochemical requirements of anodes and cathodes, which are difficult to achieve with conventional single-phase electrolytes. The BLE consisted of a cathode-customized AE (3.4 m $ZnSO_4$ in water) and an anode-customized OE (0.5 m $Zn(TFSI)_2$ in AN). Manipulating ion coordination structures and intermolecular interactions of the electrolyte couples through kosmotropic/chaotropic anions enabled on-demand control of their immiscibility/miscibility. Notably, the structural change of the AE induced by kosmotropic SO_4^{2-} allowed the phase separation with the OE, despite the good miscibility of water (in the AE) with AN (in the OE). The phase-separated, OE and AE in the BLE facilitated redox kinetics at CVO cathodes and Zn plating/stripping reversibility at Zn anodes, respectively. As a result, the BLE enabled the Zn||CVO cell to exhibit a high specific capacity (299 mA h g_{CVO}^{-1}) and a long cyclability (86.6% retention after 3500 cycles). Notably, the Zn anode-free full cell with the BLE exhibited high energy/power

densities (183/73–87/618 [W h kg^{-1}/W kg^{-1}]) along with stable capacity retention (76.7% after 100 cycles), which far outperformed those of previously reported Zn batteries. We envision that the BLE approach holds promise as a versatile electrolyte platform that can address long-unresolved performance limitations of anodes and cathodes in batteries. Furthermore, the kosmotropic/chaotropic effect-driven phase separation control can be extended to various electrolyte couples to overcome their intrinsic immiscibility/miscibility limitations.

Methods

Materials

$ZnSO_4 \cdot 7H_2O$ and $Zn(TFSI)_2$ were purchased from Junsei and Solvionic, respectively. $Ca(CH_3COO)_2$ (99%), $Zn(OTf)_2$ and $Zn(OAc)_2 \cdot 2H_2O$ were bought from Sigma-Aldrich. V_2O_5 was purchased from Pechiney. Deionized water was used for preparing aqueous electrolytes using a water purification system (Direct Q3, Millipore). Glass microfiber filters and a Cu foil modified with a graphene monolayer (gr-Cu) were purchased from Whatman and LG electronics, respectively. CVO was prepared accordingly using a previously reported microwave-assisted hydrothermal method.[33] 1 mmol of $Ca(CH_3COO)_2$ was dissolved in 20 mL ultrapure water in a glass reactor (30 mL, Anton Paar). After dissolution of $Ca(CH_3COO)_2$, 2 mmol of V_2O_5 powder was added to the reactor. The suspension was heated in a ''Monowave 300'' microwave oven (Anton Paar) up to 180 °C using the ''Heat as fast as possible'' mode and maintaining a constant temperature for 2 h at a stirring rate of 300 rpm. The obtained product was centrifuged, and the red precipitate was thoroughly washed with water and acetone. After evaporation of the residual acetone in an oven at 80 °C, the CVO powder was obtained.

Characterization

The ionic conductivity of electrolytes was measured with a conductivity meter (SevenCompact S230, METTLER TOLEDO).[11] The FTIR spectra of the electrolytes were recorded using an FTIR spectrometer (670, Varian). The immiscibility of the liquid mixtures was experimentally verified using a confocal Raman spectroscope (alpha300R, WITec). The electrolytes' wetting of the Zn metal was measured using a contact angle analyzer (Drop Shape Analysis System DSA100, Kruss) at room temperature. The surface morphologies of the samples were examined using a SEM (S4800, Hitachi). The XRD patterns were recorded using a XRD (SmartLab, Rigaku) at 45 kV and 200 mA using Cu Kα radiation. The distribution of ZnO^+ on the Zn anode was investigated by TOF-SIMS (TOF-SIMS 5, ION TOF Co.) with a Bi^+ gun (25 keV, 1.3 pA). All electrodes subjected to *ex situ* analysis after electrochemical cycling were rinsed with ethanol and dried.

Electrochemical measurements

The CVO cathode was prepared by casting a slurry mixture (CVO/carbon black/polyvinylidene fluoride) = 7/2/1 (w/w/w) in *N*-methyl-2-pyrrolidone onto a stainless steel 304 substrate, followed by vacuum drying at 60 °C for 12 h. The mass loading of active materials was 1.5–3.0 mg cm^{-2}. All cells were fabricated into CR2032 coin cells. The Zn‖CVO full cells were fabricated using the CVO cathode, Zn foil (30 μm) as the anode, glass microfiber filter as the separator and electrolytes (70 μL per cell), in which the optimal electrolyte amount (70 μL) was determined by measuring the change in bulk resistance (R_b) of the Zn‖CVO cell as a function of electrolyte amount (Fig. S38, ESI†). To prepare the Zn_xCVO cathode, the CVO electrode was pre-zincificated using Zn‖CVO cells. The Zn anode-free cells were prepared using the Zn_xCVO cathode and the commercial gr-Cu current collector after electrochemical activation. The anode-free cells were fully charged up to 1.6 V before cycling. The galvanostatic charge/discharge measurements were investigated with a cycle tester (PNE Solution Co., Ltd, Korea) at ambient temperature under various charge/discharge conditions. CV, EIS, and GITT analysis were performed with a potentiostat/galvanostat (VMP-300, Bio-Logic Science Instruments). The EIS was carried out in the frequency range from 10^{-2} to 10^6 Hz with an applied voltage of 10 mV. The GITT analysis was investigated at 100 mA g^{-1} with an interruption time between each pulse of 1 h.

Density functional theory calculations

Density functional theory (DFT) calculations were carried out using the Dmol^3 program.[50] The Becke, 3-parameter, Lee–Yang–Parr (B3LYP) functional was employed and Grimme's method[51] was used for correcting the van der Waals interactions. Double numerical basis set with polarization (DNP) functions were used with a real-space cutoff of 4.4 Å. The core electrons were explicitly treated as all electrons with relativistic effects. The self-consistent field calculation was performed with a thermal smearing of 0.005 Ha, until a convergence criterion of 1×10^{-6} Ha was satisfied. The convergence criteria for geometry optimization were set to be 1×10^{-5} Ha for energy change, 0.002 $Å^{-1}$ for the maximum force, and 0.005 for the maximum displacement. The solvent environment was described using a conductor-like screening model (COSMO).

Molecular dynamics simulations

Molecular dynamics (MD) simulations were carried out using the GROMACS 2019.5 program.[52] The general AMBER force field was used to describe the interaction between electrolyte molecules, which are $TFSI^-$, OTf^-, OAc^- anions, and AN, DEE solvents. For these molecules, the antechamber program was used to automatically generate parameters. In the case of SO_4^{2-} ions, the parameter developed by Kashefolgheta and Verde was used.[53] The TIP3P water model was used to describe the water molecules. For Zn^{2+} ions, the 12-6 Lennard-Jones potential parameter derived by Li *et al.*[54] was used. The short-range non-bonding interactions were calculated within a cutoff distance of 12 Å, and the particle mesh Ewald (PME) summation method was used to calculate electrostatic interactions. Bonded interactions with the hydrogen atoms were constrained with the LINCS algorithm. During the MD simulations, the temperature and pressure of the system were controlled using a Berendsen thermostat and a barostat, respectively. The procedures to

simulate the effect of the kosmotropic phenomenon on the phase separation of electrolytes are described in Notes S1–S5 (ESI†).

Author contributions

W. Y. K., H. I. K. and S. Y. L conceived the study. W. Y. K. and H. I. K. contributed to the design of the project and carried out the experiments. K. M. L. and E. S. performed MD simulations and DFT calculations. X. L. contributed to the chemical synthesis and analysis of CVO. H. M. conducted the Raman spectroscopy. H. A. assisted with the data analysis. S. P., S. K. K. and S. Y. L. supervised the project. All authors contributed to the discussions and preparation of the manuscript.

Conflicts of interest

There are no conflicts to declare.

Acknowledgements

This work was supported by the Basic Science Research Program (2021R1A2B5B03001615, 2021M3D1A2043791, and 2020R1A2C3005939) through the National Research Foundation of Korea (NRF) grant by the Korean Government (MSIT). This work was also supported by the LG energy solution. Computational resources were supported by the National Supercomputing Center including technical support (KSC-2020-CRE-0340) and UNIST-HPC.

Notes and references

1 M. Armand and J. M. Tarascon, *Nature*, 2008, **451**, 652–657.
2 H. Zhou, Y. Wang, H. Li and P. He, *ChemSusChem*, 2010, **3**, 1009–1019.
3 K. Xu, *Chem. Rev.*, 2004, **104**(10), 4303–4418.
4 Z. Yu, H. Wang, X. Kong, W. Huang, Y. Tsao, D. G. Mackanic, K. Wang, X. Wang, W. Huang, S. Choudhury, Y. Zheng, C. V. Amanchukwu, S. T. Hung, Y. Ma, E. G. Lomeli, J. Qin, Y. Cui and Z. Bao, *Nat. Energy*, 2020, **5**, 526–533.
5 R. Younesi, G. M. Veith, P. Johansson, K. Edström and T. Vegge, *Energy Environ. Sci.*, 2015, **8**, 1905–1922.
6 Q. Zheng, Y. Yamada, R. Shang, S. Ko, Y. Lee, K. Kim, E. Nakamura and A. Yamada, *Nat. Energy*, 2020, **5**, 291–298.
7 W. Li, H. Yao, K. Yan, G. Zheng, Z. Liang, Y. Chiang and Y. Cui, *Nat. Commun.*, 2015, **6**, 7436.
8 Y. Yamada, K. Usui, K. Sodeyama, S. Ko, Y. Tateyama and A. Yamada, *Nat. Energy*, 2016, **1**, 16129.
9 Y. Liu, D. Lin, Y. Li, G. Chen, A. Pei, O. Nix, Y. Li and Y. Cui, *Nat. Commun.*, 2018, **9**, 3656.
10 X. He, X. Liu, Q. Han, P. Zhang, X. Song and Y. Zhao, *Angew. Chem., Int. Ed.*, 2020, **59**, 6397–6405.
11 J. Chai, A. Lashgari, A. E. Eisenhart, X. Wang, T. L. Beck and J. J. Jiang, *ACS Mater. Lett.*, 2021, **3**(4), 337–343.
12 J. Meng, Q. Tang, L. Zhou, C. Zhao, M. Chen, Y. Shen, J. Zhou, G. Feng, Y. Shen and Y. Huang, *Joule*, 2020, **4**(4), 953–966.
13 S.-J. Cho, G. Y. Jung, S. H. Kim, M. Jang, D.-K. Yang, S. K. Kwak and S.-Y. Lee, *Energy Environ. Sci.*, 2019, **12**, 559–565.
14 X. Liu, X. Song, Z. Guo, T. Bian, J. Zhang and Y. Zhao, *Angew. Chem., Int. Ed.*, 2021, **60**, 16360–16365.
15 L. Cao, D. Li, T. Deng, Q. Li and C. Wang, *Angew. Chem., Int. Ed.*, 2020, **59**, 19292–19296.
16 Y. Qiao, Q. Wang, X. Mu, H. Deng, P. He, J. Yu and H. Zhou, *Joule*, 2019, **3**, 1–16.
17 N. Li, Z. Weng, Y. Wang, F. Li, H. Cheng and H. Zhou, *Energy Environ. Sci.*, 2014, **7**, 3307–3312.
18 H. Pan, Y. Shao, P. Yan, Y. Cheng, K. S. Han, Z. Nie, C. Wang, J. Yang, X. Li, P. Bhattacharya, K. T. Mueller and J. Liu, *Nat. Energy*, 2016, **1**, 16039.
19 F. Hofmeister, *Naunyn-Schmiedebergs Arch. Exp. Pathol. Pharmakol.*, 1888, **24**, 247–260.
20 K. D. Collins and M. W. Washabaugh, *Q. Rev. Biophys.*, 1985, **18**, 323–422.
21 K. D. Collins, *Biophys. J.*, 1997, **72**, 65–76.
22 F. Cheng, Q. Cao, Y. Guan, H. Cheng, X. Wang and J. D. Miller, *Int. J. Miner. Process.*, 2013, **122**, 36–42.
23 F. Wang, O. Borodin, M. S. Ding, M. Gobet, J. Vatamanu, X. Fan, T. Gao, N. Eidson, Y. Liang, W. Sun, S. Greenbaum, K. Xu and C. Wang, *Joule*, 2018, **2**, 927–937.
24 L. Miao, R. Wang, S. Di, Z. Qian, L. Zhang, W. Xin, M. Liu, Z. Zhu, S. Chu, Y. Du and N. Zhang, *ACS Nano*, 2022, **16**(6), 9667–9678.
25 D. Kundu, S. H. Vajargah, L. Wan, B. Adams, D. Prendergast and L. F. Nazar, *Energy Environ. Sci.*, 2018, **11**, 881–892.
26 P. Senguttuvan, S.-D. Han, S. Kim, A. L. Lipson, S. Tepavcevic, T. T. Fister, I. D. Bloom, A. K. Burrell and C. S. Johnson, *Adv. Energy Mater.*, 2016, **6**, 1600826.
27 H. Yang, Z. Chang, Y. Qiao, H. Deng, X. Mu, P. He and H. Zhou, *Angew. Chem., Int. Ed.*, 2020, **59**, 9377–9381.
28 X. Liu, W. Zhang, Y. Wang, W. Liu, Z. Lv and Y. Yang, *Eur. Phys. J. D*, 2018, **72**, 151.
29 D. M. Seo, O. Borodin, S.-D. Han, P. D. Boyle and W. A. Henderson, *J. Electrochem. Soc.*, 2012, **159**(9), A1489–A1500.
30 G. Y. Gor, J. Cannarella, C. Z. Leng, A. Vishnyakov and C. B. Arnold, *J. Power Sources*, 2015, **294**, 167–172.
31 M. Liu, L. Yang, H. Liu, A. Amine, Q. Zhao, Y. Song, J. Yang, K. Wang and F. Pan, *ACS Appl. Mater. Interfaces*, 2019, **11**, 32046–32051.
32 A. Naveed, H. Yang, Y. Shao, J. Yang, N. Yanna, J. Liu, S. Shi, L. Zhang, A. Ye, B. He and J. Wang, *Adv. Mater.*, 2019, **31**, 1900668.
33 X. Liu, H. Zhang, D. Geiger, J. Han, A. Varzi, U. Kaiser, A. Moretti and S. Passerini, *Chem. Commun.*, 2019, **55**, 2265–2268.
34 S. Cai, X. Chu, C. Liu, H. Lai, H. Chen, Y. Jiang, F. Guo, Z. Xu, C. Wang and C. Gao, *Adv. Mater.*, 2021, **33**, 2007470.
35 C. Szczuka, R. Eichel and J. Granwehr, *ACS Appl. Energy Mater.*, 2022, **5**(1), 449–460.
36 Y. Zhu, Y. Cui and H. N. Alshareef, *Nano Lett.*, 2021, **21**(3), 1446–1453.

37 Y. An, Y. Tian, K. Zhang, Y. Liu, C. Liu, S. Xiong, J. Feng and Y. Qian, *Adv. Funct. Mater.*, 2021, **31**, 2101886.

38 T. Foroozan, V. Yurkiv, S. Sharifi-Asl, R. Rojaee, F. Mashayek and R. Shahbazian-Yassar, *ACS Appl. Mater. Interfaces*, 2019, **11**(47), 44077–44089.

39 Y. Zhang, F. Wan, S. Huang, S. Wang, Z. Niu and J. Chen, *Nat. Commun.*, 2020, **11**, 2199.

40 L. Cao, D. Li, T. Pollard, T. Deng, B. Zhang, C. Yang, L. Chen, J. Vatamanu, E. Hu, M. J. Hourwitz, L. Ma, M. Ding, Q. Li, S. Hou, K. Gaskell, J. T. Fourkas, X.-Q. Yang, K. Xu, O. Borodin and C. Wang, *Nat. Nanotechnol.*, 2021, **16**, 902–910.

41 H. Qiu, X. Du, J. Zhao, Y. Wang, J. Ju, Z. Chen, Z. Hu, D. Yan, X. Zhou and G. Cui, *Nat. Commun.*, 2019, **10**, 5374.

42 D. Han, C. Cui, K. Zhang, Z. Wang, J. Gao, Y. Guo, Z. Zhang, S. Wu, L. Yin, Z. Weng, F. Kang and Q.-H. Yang, *Nat. Sustain.*, 2022, **5**, 205–213.

43 T. Xiong, Y. Zhang, Y. Wang, W. S. V. Lee and J. Xue, *J. Mater. Chem. A*, 2020, **8**, 9006–9012.

44 D. Chao, C. Zhu, M. Song, P. Liang, X. Zhang, N. H. Tiep, H. Zhao, J. Wang, R. Wang, H. Zhang and H. J. Fan, *Adv. Mater.*, 2018, **30**, 1803181.

45 Y. Jiao, F. Li, X. Jin, Q. Lei, L. Li, L. Wang, T. Ye, E. He, J. Wang, H. Chen, J. Lu, R. Gao, Q. Li, C. Jiang, J. Li, G. He, M. Liao, H. Zhang, I. P. Parkin, H. Peng and Y. Zhang, *Adv. Funct. Mater.*, 2021, **31**, 2107652.

46 W. Li, K. Wang, M. Zhou, H. Zhan, S. Cheng and K. Jiang, *ACS Appl. Mater. Interfaces*, 2018, **10**(26), 22059–22066.

47 Z. Wang, J. Huang, Z. Guo, X. Dong, Y. Liu, Y. Wang and Y. Xia, *Joule*, 2019, **3**, 1289–1300.

48 W. Li, K. Wang, S. Cheng and K. Jiang, *Adv. Energy Mater.*, 2019, **9**, 1900993.

49 N. Wang, X. Dong, B. Wang, Z. Guo, Z. Wang, R. Wang, X. Qiu and Y. Wang, *Angew. Chem., Int. Ed.*, 2020, **59**, 14577–14583.

50 B. Delley, *J. Chem. Phys.*, 1990, **92**, 508–517.

51 S. Grimme, *J. Comput. Chem.*, 2006, **27**, 1787–1799.

52 D. V. D. Spoel, E. Lindahl, B. Hess, G. Groenhof, A. E. Mark and H. J. C. Berendsen, *J. Comput. Chem.*, 2005, **26**, 1701–1718.

53 S. Kashefolgheta and A. V. Verde, *Phys. Chem. Chem. Phys.*, 2017, **19**, 20593–20607.

54 P. Li, B. P. Roberts, D. K. Chakravorty Jr. and K. M. Merz, *J. Chem. Theory Comput.*, 2013, **9**, 2733–2748.